JOINT INVERSION FOR CRUSTAL AND UPPER-MANTLE SHEAR-WAVE VELOCITY AND ATTENUATION STRUCTURE IN EASTERN EURASIA USING THREE-DIMENSIONAL FULL-WAVE FRÉCHET KERNELS

Po Chen[2], Youlin Chen[1], and Winston Chan[1]

Array Information Technology[1] and University of Wyoming[2]

Sponsored by the Air Force Research Laboratory

Award No. FA9453-10-C-0215
Proposal No. BAA10-06

ABSTRACT

We aim to map the lateral variations of crustal and upper-mantle shear-wave velocity β and shear attenuation ($1/Q_\mu$) in eastern Eurasia using a new joint inversion procedure based on three-dimensional (3D) sensitivity (Fréchet) kernels. In the first year of this project, we analyzed thousands of Rayleigh wave recordings with periods longer than ~15 s, derived from more than 250 regional and near-teleseismic earthquakes that occurred within our study region (10°–60°N, 70°–140°E). The data were recorded on the broadband seismic stations in this region, including the Chinese National Digital Seismic Network. The seismograms were evaluated for signal-to-noise within the band of interest (10–80 mHz) by comparing the records to complete synthetic seismograms computed using a 3D reference model derived from receiver-function analysis. We then made mutually consistent measurements of frequency-dependent phase-delay time and amplitude anomalies for surface waves by cross-correlation between records and synthetics. We used the spectral-element code to compute the 3D Fréchet kernels of these travel-time and amplitude anomalies to both the elastic shear-wave speeds β and shear-wave quality factor Q_μ values. Our starting model for Q_μ was extracted from a recent global model of upper-mantle attenuation. The frequency-dependent travel-time and amplitude anomalies were jointly inverted for 3D models of both elastic and anelastic structures. This coupled inversion allowed us to account for the effects on amplitudes from elastic heterogeneities such as scattering, focusing and defocusing, as well as the effects of anelastic dispersion on the travel times. Our primary models provide lateral resolution of about 400 km in the crust and upper mantle. In the crust, high values of Q_μ are concentrated in eastern China, extending southward from the North China craton, while a clear low-Q anomaly exists in the crust beneath northern Tibet. In the upper mantle, the model is characterized by a lithosphere with very high Q values ranging from 250 to 400, underlain by a low-Q asthenosphere with Q_μ of 60–100. The lateral variation of the upper-mantle Q_μ perturbation appears to correlate with the lateral variation in the inverted shear-velocity perturbation.

OBJECTIVES

The objectives of this project are to jointly invert for 3D seismic velocity and shear attenuation for the crust and upper mantle in eastern Eurasia using 3D full-wave Fréchet kernels. In this study, we analyze broadband surface waves from regional earthquakes, recorded on stations of the Chinese National Digital Seismic Network (CNDSN) and IRIS Global Seismic Network (GSN), and measure amplitude and phase residuals of these waveforms with respect to synthetics calculated from a 1D reference Earth model that represents the eastern Eurasia region using the Generalized Seismological Data Functionals (GSDF) method. These observations are then inverted for a 3D tomographic model of shear velocity (β) and shear attenuation ($1/Q_\mu$), using 3D Fréchet kernels that fully account for the effects of both elastic and anelastic structure on the amplitude and phase measurements. By jointly inverting for β along with $1/Q_\mu$, we remove much of the uncertainty associated with focusing and defocusing that is typically found in previous attenuation models. Our inverted attenuation perturbation (δQ_μ^{-1}) has a spatial correlation with our inverted shear-velocity perturbation ($\delta\beta$), which may suggest that the lateral variation in attenuation in the crust and upper mantle in eastern Eurasia is a result of temperature variation.

RESEARCH ACCOMPLISHED

Background

The eastern part of the Eurasian continent is characterized by a complex tectonic history. This region is composed of three major Precambrian cratons with very different origins: the Sino-Korean craton, the Yangtze craton, and the Tarim craton (Figure 1).

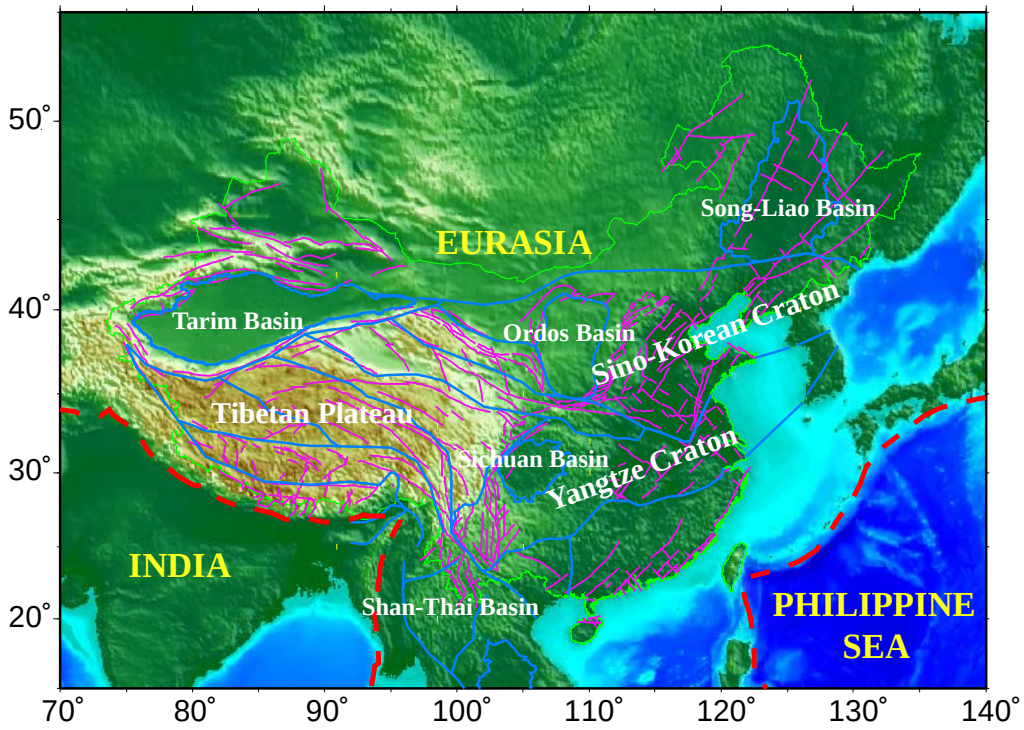

Figure 1. Tectonic setting in eastern Eurasia. Active faults are shown as purple lines and tectonic sutures are shown in blue lines. This part of Eurasia is being pushed in the south by the Indian plate and in the east and southeast by the Pacific and Philippine Sea plates, respectively.

The modern tectonics in this region is the result of a long and complicated evolution history of collision, underthrust, and suture between different tectonic blocks (e.g., Molnar and Tapponnier, 1975; Yin and Nie, 1996; Yin and Harrison, 2000; Vermeesch 2003). A good tomographic image of the crustal and upper-mantle structure would be very helpful in understanding these complexities. Indeed this region has been the focus in many previous regional and global tomographic studies of seismic velocity structures using surface waves (e.g., Song et al., 1991; Wu et al., 1997; Xu et al., 2000; Shapiro and Ritzwoller, 2002; Friederich, 2003; Huang et al., 2003; Lebedev and Nolet, 2003), S_n waves (e.g., Ritzwoller et al., 2002; Pei et al., 2007), receiver functions (e.g., Wu et al., 2001; Zou and Chen, 2003; Xu et al., 2006; Chen et al., 2010), and body-wave travel times (Sun and Toksöz., 2006; Sun et al., 2008).

Attenuation ($1/Q$) tomography for anelastic structure may provide additional constraints for the tectonics in eastern Eurasia. Considering the different sensitivities of seismic velocity and Q to temperature and composition (e.g., Karato, 1993; Faul and Jackson, 2005), a joint interpretation of both attenuation and velocity models would be very helpful in distinguishing the effects of thermal and chemical heterogeneities. Q is known to vary widely in continental regions, making its reliable estimates critically important but also quite difficult. Q is also frequency dependent, which makes it difficult to determine whether Q estimates derived from different phases with different frequency characteristics are a result of intrinsic frequency dependence or differences in structural sampling. Finally, Q estimates are derived from seismic amplitudes, which are also strongly dependent on elastic effects such as wavefield focusing and scattering. We address the difficulties in attenuation tomography by applying a unified waveform analysis and inversion method to simultaneously infer 3D seismic velocity and attenuation structures.

Waveform Data

We adopt broadband waveforms recorded on CNDSN stations, complemented by those on IRIS-GSN stations. Since the 1990s, the China Earthquake Administration (CEA) has made a great effort to upgrade its seismic instruments from analog to digital in order to establish a modern seismic network at a national level. The effort resulted in the number of modern digital seismic stations in the backbone network of China increasing from 11 GSN stations in the 1990s to 75 stations established in the early 2000s and the current 145 stations deployed since 2007.

Most CNDSN stations are equipped with the Chinese broadband seismographs, such as JCZ-1, CTS-1, and FBS-3, which have been well calibrated and tested by the Chinese seismological community (e.g., Lin, 2001; Zhao et al., 2001; Xie and Zhao, 2003). All of these instruments are broadband and have velocity-flat response. The upper bounds of their bandwidths are over 20 Hz, and the lower bounds are down to 360 seconds. The sampling rates are 50 samples per second, and the dynamic ranges are greater than 120 dB. In this study, we have included waveform data from 68 CNDSN stations, which increases the total number of stations in our tomography region from 46 to 114 (Figure 2). All of these 68 stations were updated in early 2000s and have accumulated large volumes of high-quality waveform data.

Seismograms from 848 earthquakes with $5.0 \leq Mw \leq 6.5$ and occurring in the region 10°N–60°N and 70°E–140°E from 2000 to 2008 (Figure 2) are selected, and those with sufficiently high signal-to-noise ratio are processed. The two horizontal components are rotated into the radial and transverse directions. The resulting seismograms are then low-pass filtered using a 4th-order Butterworth filter with corner frequency at 50 mHz. Examples of the processed vertical-component observed seismograms from an Mw5.9 earthquake occurring in 2005 and recorded at 18 CNDSN stations are shown in Figure 3.

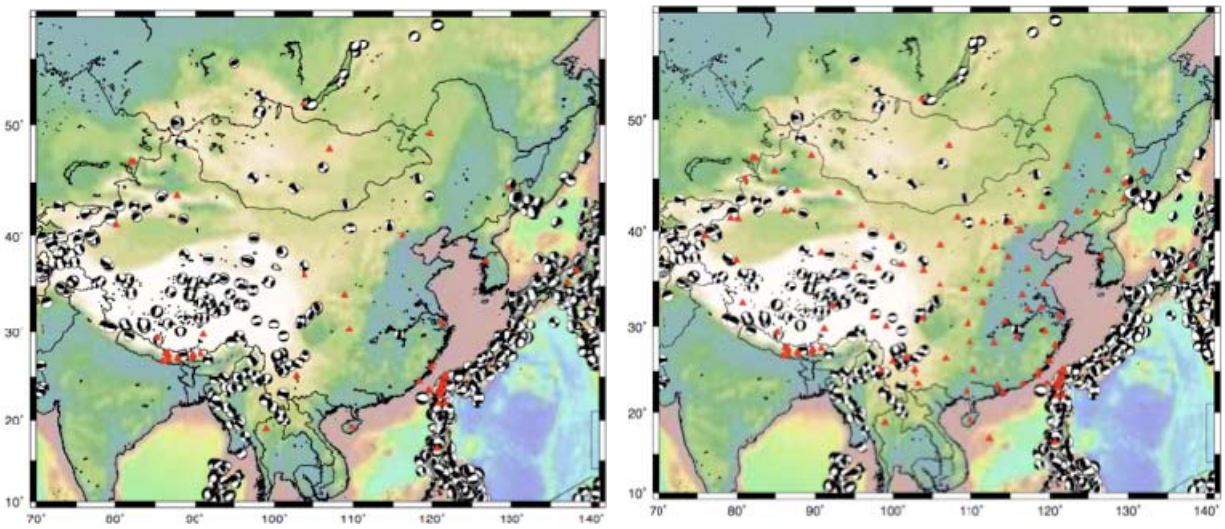

Figure 2. Station coverage within our tomography region with (right) and without (left) the CNDSN stations. Red triangles: Seismic stations, 41 in left panel and 114 in right panel. Beach balls: Harvard CMT solutions of 848 earthquakes with M_w>5.0 from year 2000 to 2008. Background color shows topography.

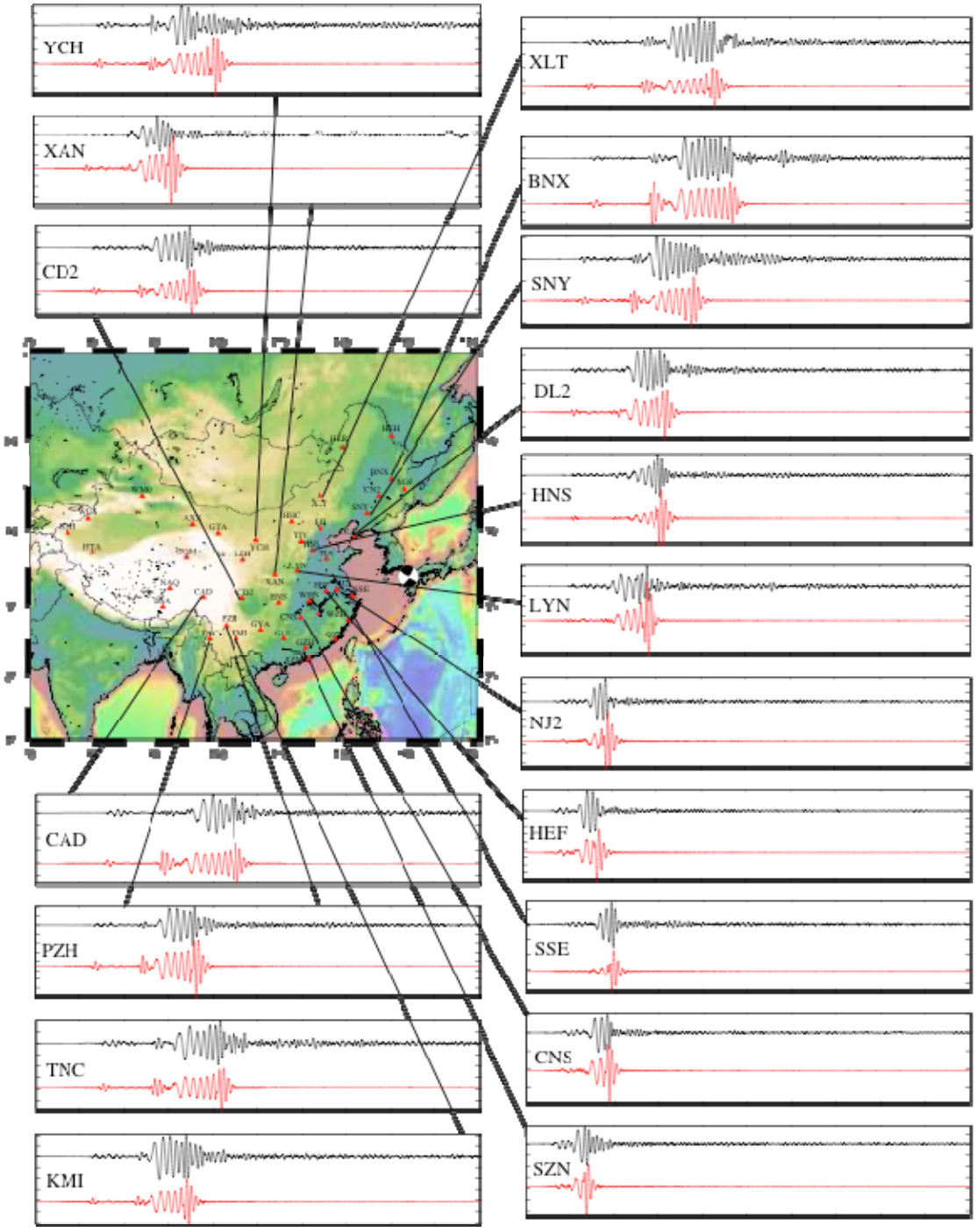

Figure 3. Examples of observed (black) and synthetic (red) vertical-component seismograms at 18 CNDSN stations. The seismograms have been low-pass filtered using a Butterworth filter with a corner at 50 mHz. The synthetics were computed using the 1D structure model, as shown in Figure 4, and a normal-mode summation code. The focal mechanism of the earthquake is obtained from the Harvard CMT catalog.

Methodology

We formulate our tomography as an optimization problem, in which we optimize the Earth structure model **m** to minimize an objective function defined in terms of the misfit between the observation and the model prediction with three regularization terms:

$$\chi^2 = \|\mathbf{d}\| + \lambda_1 \|\mathbf{m}\| + \lambda_2 \|\mathbf{Lm}\| + \lambda_3 \|\mathbf{m}_0 - \mathbf{m}\| . \quad (1)$$

Here the first term on the right-hand side quantifies waveform misfit between observed and synthetic seismograms, the second term regularizes the amplitude of the model, the third term regularizes the smoothness of the model, and the fourth term is used to impose additional constraints on certain portions of the model or to force the solution toward a certain direction. The Lagrangian multipliers $\lambda_{1,2,3}$ control the trade-off between fitting the seismic data and the three regularization terms.

Reference Model and Synthetic Seismogram

In the current study, we adopt a 1D structure model (Figure 4) as our reference model. The velocity model was constructed from a composition of iasp91 for mantle shear and compressional velocities and Crust 2.0 (Laske et al., 2001) for local crustal velocity perturbations. The attenuation model was composed of a mantle Q_μ profile extracted from the recent global attenuation model (Dalton and Ekström, 2006) and a crustal Q_μ profile derived from analysis of regional phases (Jemberíe and Mitchell, 2004). In order to accomplish our purpose of full 3D tomography, we will adopt a 3D reference model over eastern Eurasia derived from receiver function analysis made on each station.

For such a spherically symmetric reference earth model, complete synthetic seismograms can be computed using normal mode superposition (Dalen and Tromp, 1998). Centroid moment tensor (CMT) solutions from the global CMT catalog are used as our source models for computing synthetics. The calculated synthetic seismograms are convolved with corresponding instrument responses. Figure 3 shows a comparison between some vertical-component synthetic seismograms and their corresponding observed seismograms. For frequency up to 50 mHz, our synthetic seismograms generally provide sufficiently good fit to the observed seismograms, which indicates that our composite 1D structure model provides a good reference model for our tomographic inversion.

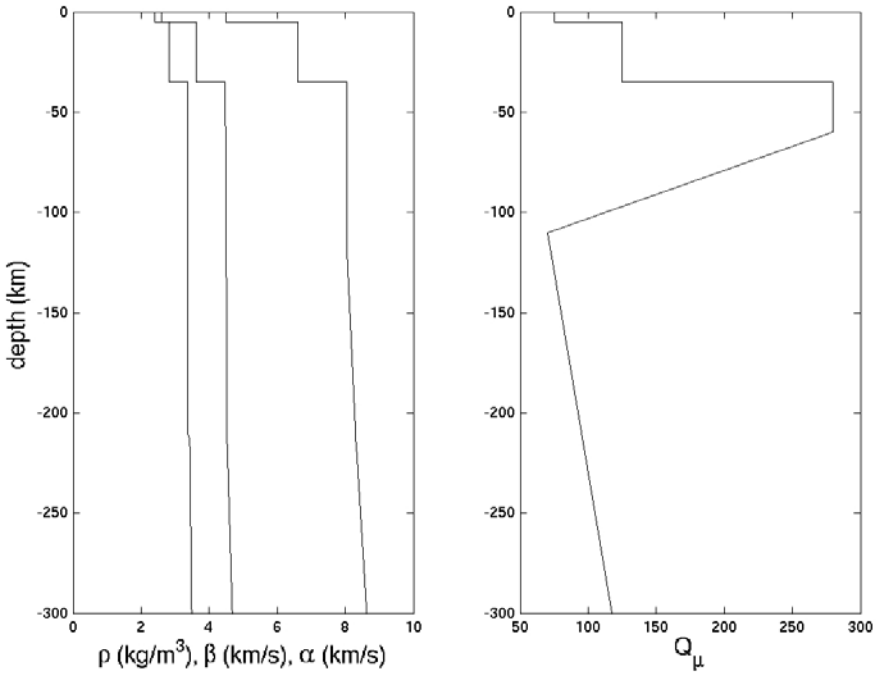

Figure 4. The 1D reference structure model used in our inversion. Left: The density, shear- and compressional-wave speeds as functions of depth. Right: Shear-attenuation quality factor as a function of depth.

Generalized Seismological Data Functionals (GSDF)

The misfit measurement **d** in Equation (1) is defined as the frequency-dependent phase-delay time and amplitude reduction time introduced in Gee and Jordan (1992) under the term Generalized Seismological Data Functionals (GSDF). The GSDF measurements generalize the classic travel-time and t^* measurements to better capture differences in the shapes of the waveforms.

In the frequency domain, we can map the synthetic waveform $u_i(\omega)$ into the observed waveform $\overline{u}_i(\omega)$ using two frequency-dependent, time-like quantities: the phase-delay times $\delta\tau_p(\omega)$ and the amplitude-reduction times $\delta\tau_q(\omega)$:

$$\overline{u}_i(\omega) = u_i(\omega)\exp\left\{i\omega\left[\delta\tau_p(\omega) + i\delta\tau_q(\omega)\right]\right\}. \quad (2)$$

To make the GSDF measurements, we first segment the complete synthetic seismogram to isolate the wave group that is to be measured. The isolated wave group is termed "isolation filter" (Figure 5b), which can contain any types of seismic phases. The isolation filter is then cross-correlated with both the observed seismogram and the complete synthetic seismogram (Figures 5c and d). The resulting cross-correlagrams are then windowed around zero-lag and narrow-band filtered at a set of frequencies of interest. After the narrow-band filtering operation, the resulting cross-correlagrams can be well parameterized using a five-parameter Gaussian wavelet (Gabor function). The amplitude and phase differences between the data and the synthetic wavelets provide us the frequency-dependent phase-delay measurements $\delta t_p(\omega_n)$ and amplitude anomaly $\delta t_q(\omega_n)$ at each narrow-band filtering frequency ω_n (Figures 5e and g). The misfit measurements of $\delta t_x(\omega_n)$ (x = p, q) are weighted averages of $\delta\tau_x$ over narrow frequency-bands centered on the narrow-band filtering frequency ω_n. The effects of the averaging introduced by our measurement procedure are completely accounted for in our full-wave Fréchet kernels (Chen et al., 2010).

The GSDF analysis has several advantages that are important to our tomographic inversion. First, a direct benefit of using frequency-dependent cross-correlation measurements is that the spatial sampling patterns of the associated Fréchet kernels are also frequency-dependent (Figure 6), which provides more spatial resolution than the kernels for a single broadband cross-correlation measurement (Gaherty et al., 1996; Katzman et al., 1998; Chen et al., 2007). Second, as shown in Figure 5c (green line), these frequency-dependent GSDF measurements can effectively capture the shape of the waveforms if the sampling in frequency domain is dense enough. Third, these GSDF measurements are well suited for the tomographic inverse problem. In particular, their linearization is based on the Rytov approximation, which is valid for large *accumulative* phase shifts as long as the phase perturbation *per wavelength* is small (Chernov, 1960; Snieder and Lomax, 1996).

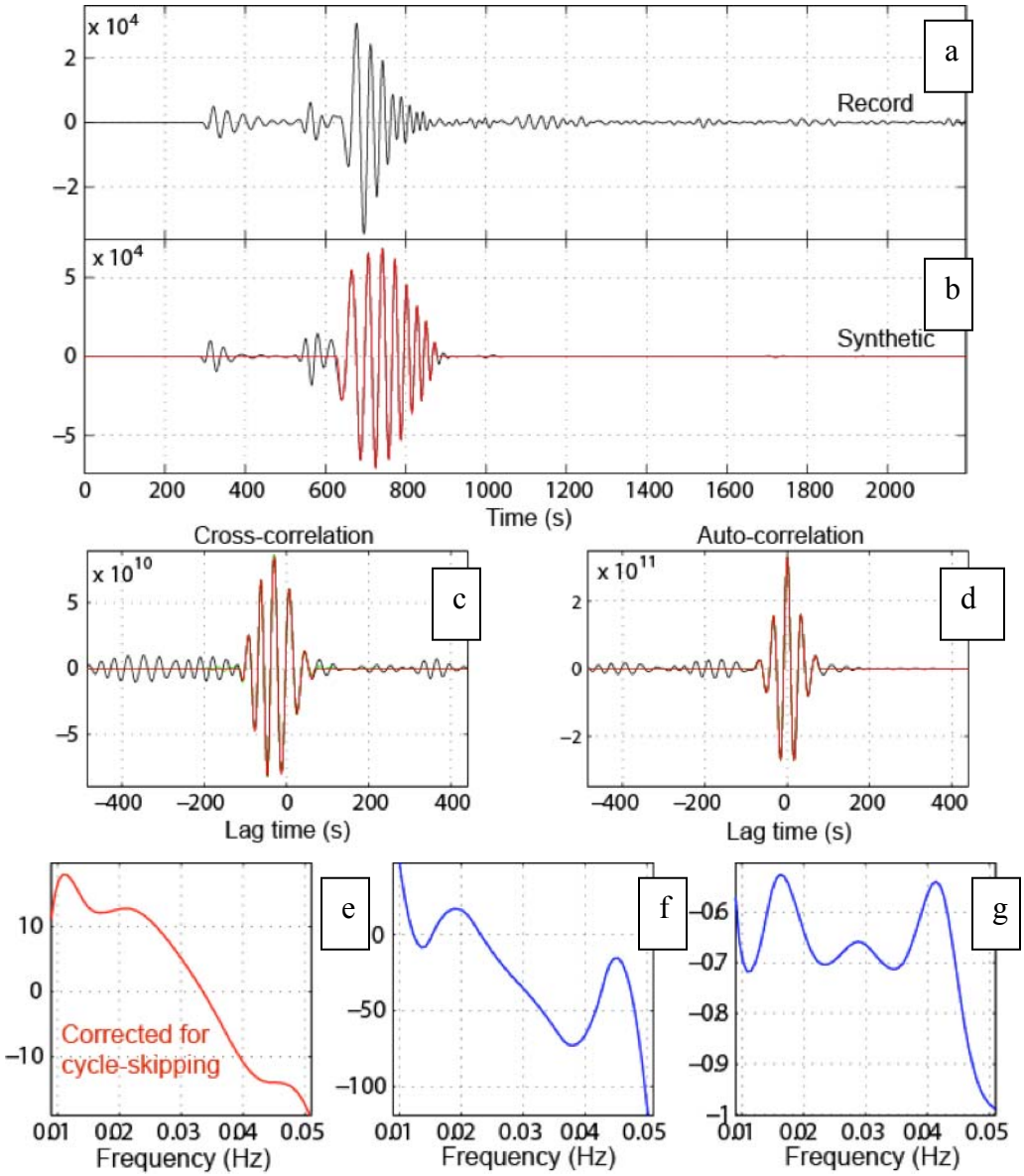

Figure 5. Our waveform analysis procedure, which follows Gee and Jordan (1992), for extracting frequency-dependent phase-delays and amplitude anomalies from waveforms. (a) Observed seismogram. (b) Synthetic seismogram (black) and the isolation filter (red), which includes the surface wave. (c) Cross-correlagram between the isolation filter and the observed seismogram (black), the windowed cross-correlagram (red) and the one recovered from the synthetic by applying the frequency-dependent phase-delay and amplitude anomaly using the right-hand side of Equation 2 (green). (d) Cross-correlagram between the isolation filter and the complete synthetic seismogram (black) and the windowed cross-correlagram (red). (e) Frequency-dependent phase-delay time. (f) Frequency-dependent group-delay time. (g) Frequency-dependent amplitude anomaly.

Three-Dimensional Full-Wave Fréchet Kernel

In this study, we adopt the normal-mode coupling theory (Zhao et al., 2000; Zhao and Jordan, 2006) for computing Fréchet kernels of our frequency-dependent GSDF measurements. The mode-coupling approach is a complete full-wave method and provides accurate 3D Fréchet kernels for any arrivals in both far field and near field in 1D reference models.

Following the notation in Zhao and Jordan (2006), the Born approximation to waveform perturbation can be expressed as

$$\delta\mathbf{u}(\mathbf{r}_R, t; \mathbf{r}_S) = \int_{\oplus}\int_{-\infty}^{\infty} [\nabla\mathbf{G}_0(\mathbf{r}_R, \tau; \mathbf{r})] : \delta\mathbf{\Lambda}(\mathbf{r}) : [\nabla\mathbf{u}_0(\mathbf{r}, t-\tau; \mathbf{r}_S)]\, d\tau\, d^3\mathbf{r}, \quad (3)$$

where $\delta\mathbf{\Lambda}(\mathbf{r})$ represents perturbations in structural parameters, $\mathbf{G}_0(\mathbf{r}_R, \tau; \mathbf{r})$ is the Green's tensor from the scattering point $\mathbf{r}$ to the receiver location $\mathbf{r}_R$, and $\mathbf{u}_0(\mathbf{r}, t-\tau; \mathbf{r}_S)$ is the forward wavefield from the source location $\mathbf{r}_S$ to the scattering point $\mathbf{r}$. It would take some time if both the Green's tensor and the forward wavefield were computed by normal-mode summation, and since we need to compute the kernels for a large number of points in space, this can make the whole calculation impractical for tomography. So our approach is to compute the Green's tensors in the reference model for a densely populated grid points, and store all the Green's tensors in a database. Then, when we need to compute the kernel for an arbitrary measurement, we can simply find the appropriate Green's tensors in the database and retrieve them. This makes the kernel calculations practical for tomography.

Figure 6 shows examples of our 3D full-wave Fréchet kernels for a shallow earthquake at 21-km depth. These kernels are computed for GSDF measurements at 20 mHz and 40 mHz made on the vertical-component Rayleigh wave. The figure shows cross sections of the kernels near the surface, and we can see that the symmetry across the source-receiver great-circle path is broken by the radiation pattern from the CMT solution. The width of the Fresnel zone depends on the frequency at which the measurements are made and is narrower at higher frequency. The kernels of the amplitude measurements with respect to P- and S-wave speeds allow us to correctly account for elastic effects on amplitudes, such as focusing/defocusing, in our velocity-attenuation joint inversion.

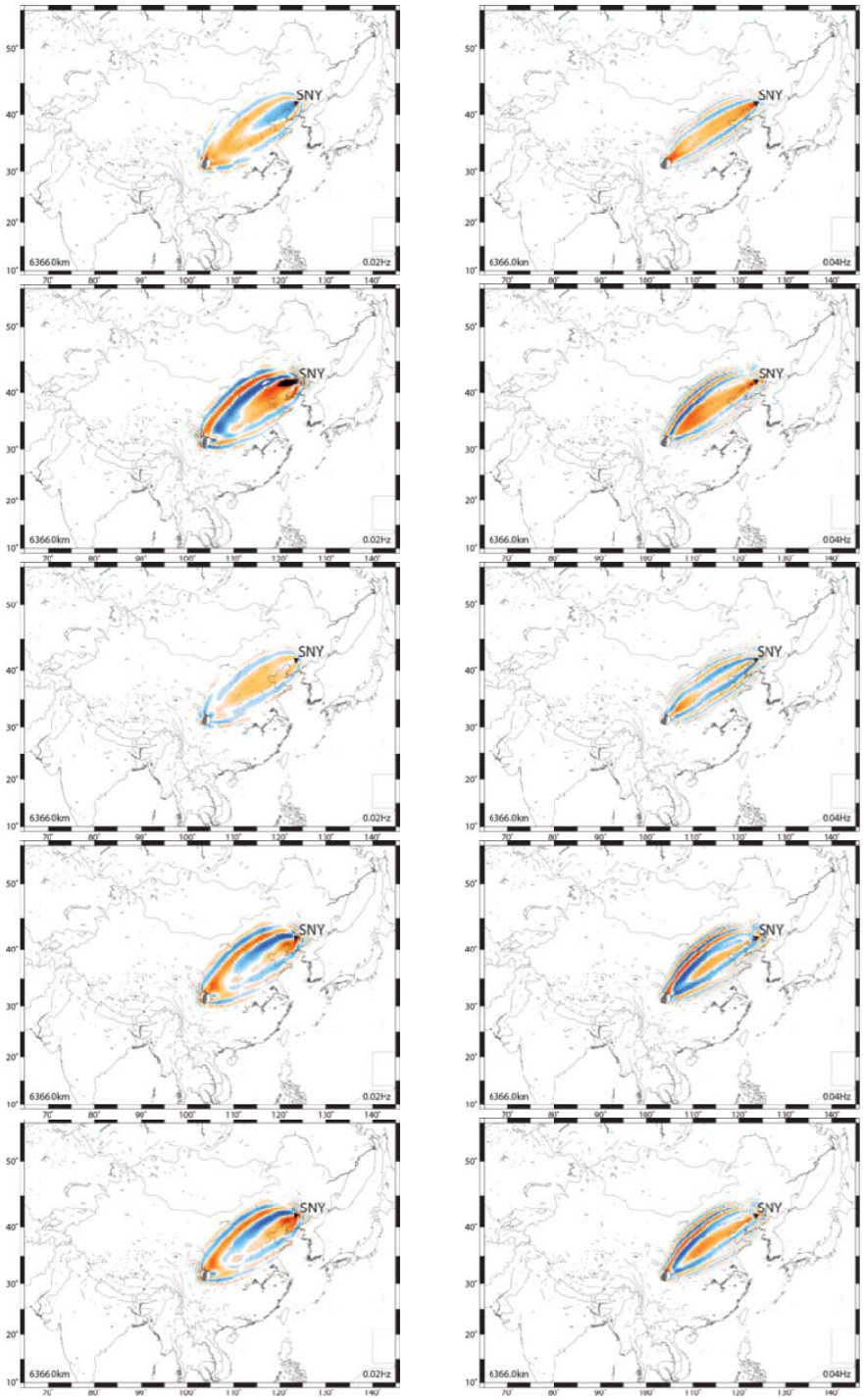

Figure 6. Examples of our 3D full-wave Fréchet kernels for an earthquake at 21-km depth. The left column shows the kernels for phase-delay and amplitude anomaly measured at 20 mHz, and the right column shows the kernels for measurements made at 40 mHz. The top two rows show the kernels for phase-delay measurements with respect to P- and S-wave speeds. The next three rows show kernels for amplitude anomalies with respect to P- and S-wave speeds and shear attenuation ($1/Q_\mu$). The beach ball shows the CMT solution for the earthquake.

Inversion

Optimizing Equation (1) using the Gauss-Newton algorithm requires the solution of the Gauss-Newton normal equation, which can be obtained by solving the following linear system:

$$\begin{bmatrix} \mathbf{C}_{\mathrm{d}}^{-1/2}\mathbf{A} \\ \mathbf{C}_{\mathrm{m}}^{-1/2} \end{bmatrix} \delta\mathbf{m} = \begin{bmatrix} \mathbf{C}_{\mathrm{d}}^{-1/2}\mathbf{d} \\ 0 \end{bmatrix} \tag{4}$$

by using the LSQR algorithm (Paige and Saunders, 1982). Here matrix **A** contains the sensitivity kernels for each misfit measurement, $\delta\mathbf{m}$ is the model parameter vector, **d** is the misfit measurement data vector, $\mathbf{C}_{\mathrm{d}}^{-1/2}$ is a data-weighting matrix, and $\mathbf{C}_{\mathrm{m}}^{-1/2}$ is a "roughing operator," which is a linear combination of the Laplacian operator (Constable et al., 1987; Sambridge, 1990) and the identity operator, i.e., $\mathbf{C}_{\mathrm{m}}^{-1/2} = \theta(\mathbf{I} + \lambda\nabla^2)$. Using this definition of the "roughing operator," we impose our prior information on the inversion; i.e., we assume that in the absence of any other information, the model perturbation is smooth and small.

Effect of P-wave Speed on Rayleigh Waves

We are mainly concerned with S-wave speed and shear attenuation ($1/Q_\mu$), and most of our GSDF measurements are made on surface waves. It has been recognized for many years that the P-wave speed, especially the P-wave speed in the crust, affects the surface wave phase and group velocities. But to our knowledge, the effect of P-wave speed on Rayleigh waves has not been explicitly considered in surface wave tomography so far. In Figure 7, we illustrate the effect of P-wave speed on Rayleigh waves through an example.

Figure 7 shows two pairs of Rayleigh waves in two different frequency bands at 60 degrees distance. In each pair, the black line is the Rayleigh wave for model AK135, and the red line is the Rayleigh wave for a model that is obtained by replacing the P-wave structure in the upper 800 km of AK135 with the corresponding P-wave structure in PREM. So there is no difference in S-wave speed between the two structure models, but we see that the Rayleigh waves are shifted by about 8 seconds. This example demonstrates that surface wave phase-delay anomalies may come entirely from perturbations in P-wave speed. So in this study, we take the P-wave speed into account for Rayleigh wave measurements. Examples of our full-wave Fréchet kernels for Rayleigh wave phase-delay and amplitude measurements with respect to P-wave speed are given in Figure 6.

Resolution Analysis

The modeling domain is from 0.5°N to 69°N in latitude, from 54.5°E to 157°E in longitude and from 0 km to 300 km in depth (Figure 8). The entire modeling domain is discretized into 0.5-degree by 0.5-degree cells horizontally and divided unevenly into 23 layers vertically, resulting in 645,955 blocks. Considering perturbations in P- and S-wave speeds and shear attenuation ($1/Q_\mu$), the total number of model parameters is 1,937,865. In this study, we used surface waves from 1,707 source-station paths that provide excellent coverage of our modeling domain. For each surface wave, we made GSDF measurements at nine frequencies evenly distributed from 10 mHz to 50 mHz, with 5 mHz intervals, resulting in 15,363 frequency-dependent phase-delay measurements and amplitude anomalies. The resulting linear system as specified in Equation (4) was then solved using a parallelized LSQR subroutine from the PETSc parallel scientific computing library (Balay et al., 2004).

To investigate the resolution of our inversion, we carried out a series of checkerboard tests with different cell sizes. An example of our checkerboard tests is shown in Figure 8. The recovery of the checkerboard pattern is better at shallower depths. The resolution for P-wave speed becomes worsening at and below about 66-km depth, while the resolution for S-wave speed and shear attenuation remains good in easternmost part of the model down to at least 300 km. The results of these checkerboard tests suggest that the smallest horizontal scale that our inversion can resolve is around 600 km.

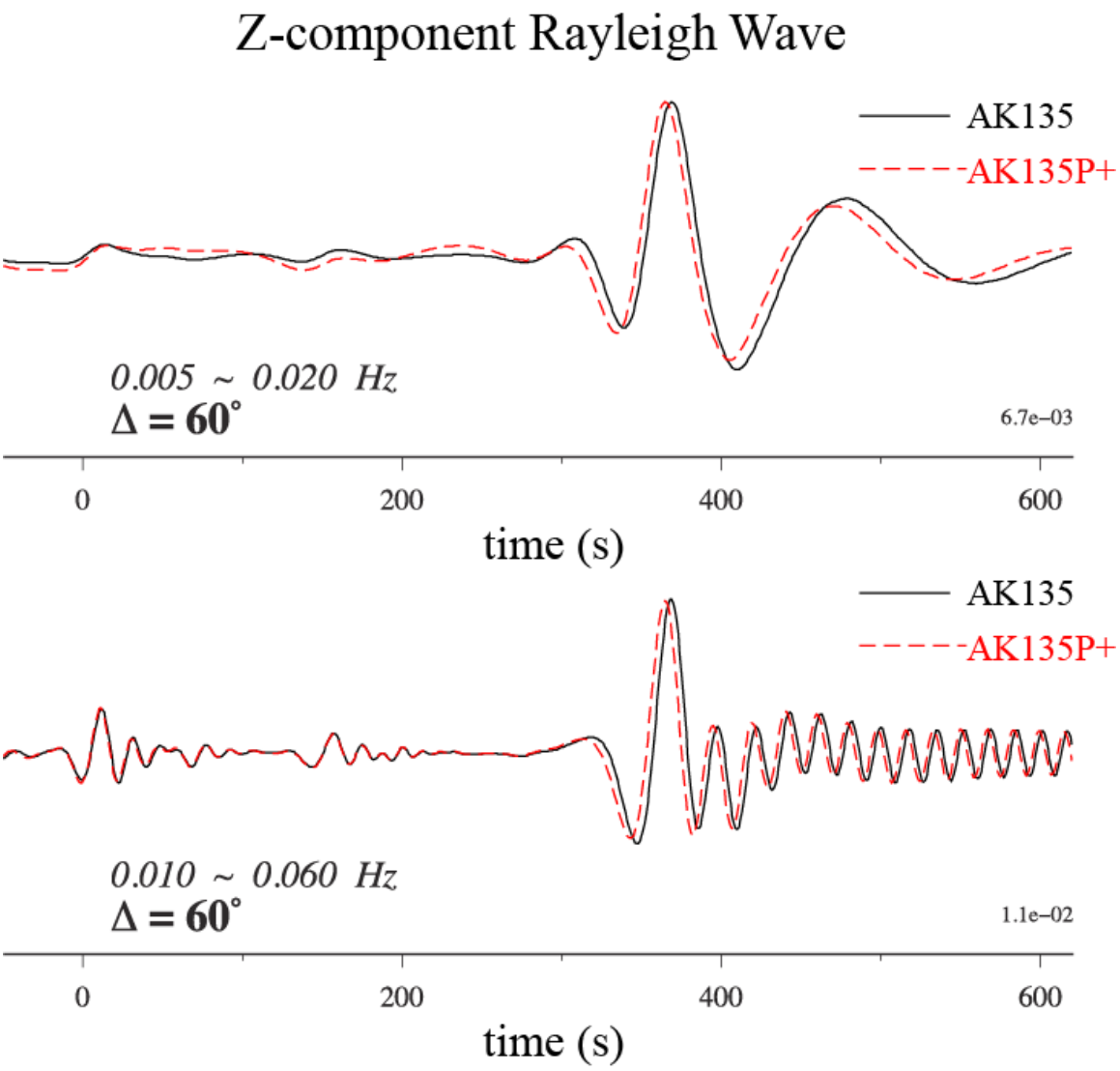

Figure 7. The effect of P-wave speed perturbation on Rayleigh wave phase-delay time. Black lines: Rayleigh waves generated using AK135. Red lines: Rayleigh waves generated using a model AK135P+ obtained by replacing the upper-800-km P-wave speed in AK135 with that of PREM. Upper plot: The two Rayleigh waves band-pass filtered from 5 mHz to 20 mHz. Lower plot: The two Rayleigh waves band-pass filtered from 10 mHz to 60 mHz.

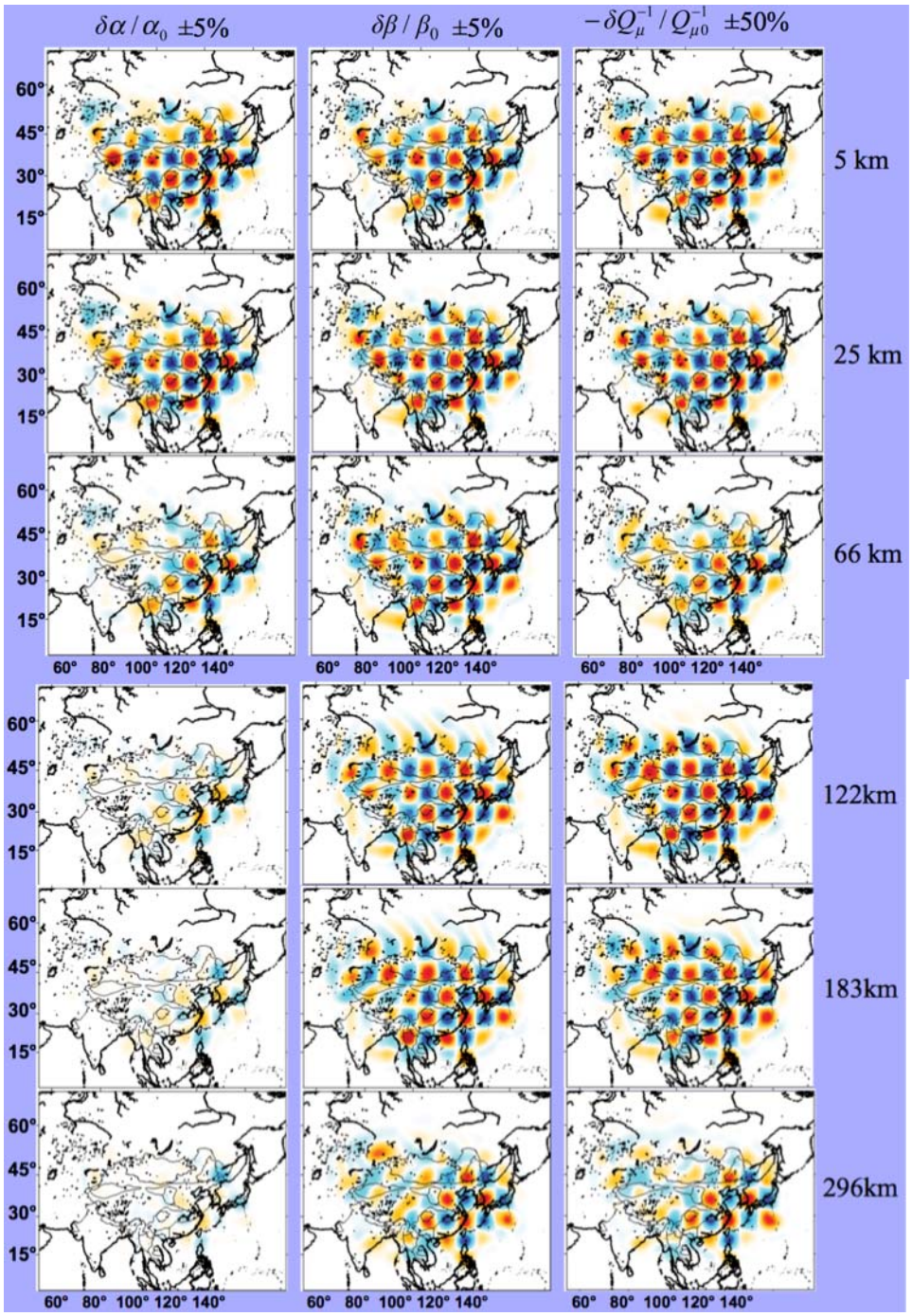

Figure 8. An example of our resolution tests showing the recovery of checkerboards for P- (left column) and S-wave (middle column) speeds and shear attenuation (right column) at six different depths. The input checkerboard has 5% perturbation for P- and S-wave speeds and 50% perturbation for shear attenuation.

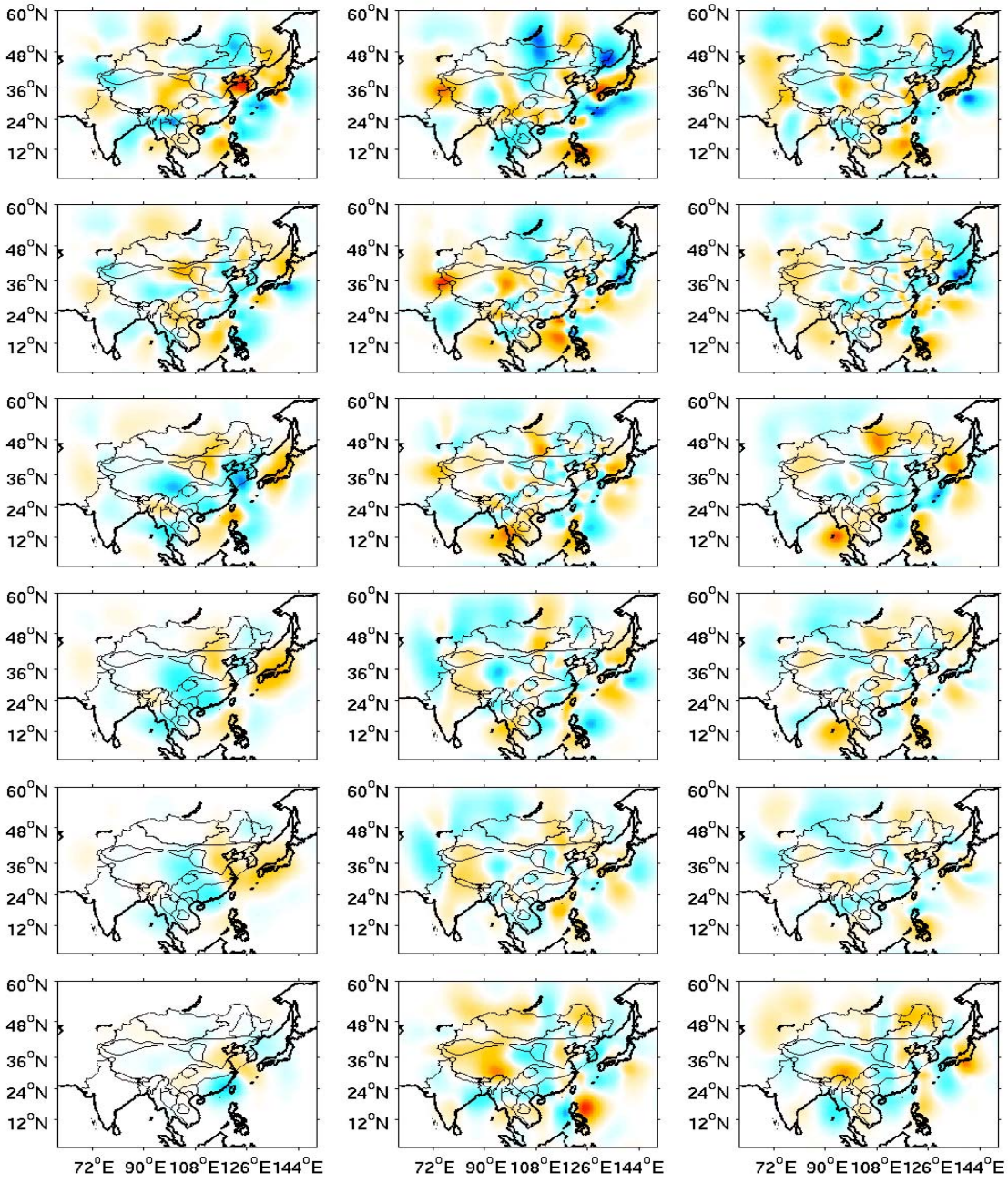

Figure 9. Our tomography models for the perturbations of P- (left column) and S-wave (middle column) speeds and shear attenuation (right column) at six different depths. There seems to be an overall positive correlation between S-wave speed and Q_μ. We see that the blue high-speed region corresponds to the blue region for low attenuations in the model, and we see the low S-speed region corresponds to high attenuation in the Q_μ model. There doesn't seem to be such correlation between the P- and S-wave speed models.

CONCLUSIONS AND RECOMMENDATIONS

The shear-velocity and shear-attenuation perturbations obtained from our preliminary inversion (Figure 9) seem to be geologically plausible. A major feature of our inverted Q_μ perturbation is that at shallower depth in the lithosphere, the average perturbation is positive, while at larger depths in the asthenosphere, the average perturbation is negative. This inverted Q_μ perturbation seems to enhance the depth gradient that already exists in our 1D reference model (Figure 4). In lower crust to upper mantle, the lateral variation of the inverted Q_μ perturbation shows a strong negative anomaly in northern Tibet and increases towards south and east. This lateral variation in Q_μ perturbation also seems to correlate with the lateral variation in the inverted shear-velocity perturbation. This result seems to be consistent with the conclusion reached by Xie (2006) based on spectral analysis on Pn arrivals from 1 to 10 Hz. In Xie (2006) this lateral variation of attenuation was interpreted as a result of temperature variation in the mantle lid under Tibet; i.e., the temperature in the mantle lid under northern Tibet is abnormally high and causes partial melting while it is abnormally low under southern and eastern Tibet due to the underthrusting Indian lithosphere.

In this study we have derived a 3D shear velocity and attenuation model for eastern Eurasia by inverting frequency-dependent phase-delay and amplitude anomalies measured on surface waves. Compared with previous surface wave tomographic inversions in the same region, we have made four major improvements in our approach. First, by including seismic stations from the CNDSN, we greatly enhanced source-station path coverage for our tomography region, which proved to be essential in improving the resolution of our inversion results. Second, the GSDF analysis provides an effective means to utilize waveform data. In particular, it converts waveform misfits, which are highly nonlinear with respect to structural parameters, into frequency-dependent phase-delays and amplitude anomalies, which are only weakly nonlinear and can be effectively linearized with respect to structural parameters. Third, by including both P- and S-wave speeds together with shear attenuation in a joint inversion, we were able to correctly account for the effect of P-wave speed on Rayleigh wave phase-delays and elastic effects on surface wave amplitudes. Fourth, we have developed an efficient algorithm for computing 3D full-wave Fréchet kernels based on the Green's tensor database, which is computed by normal-mode summation and accounts for the full physics of wave interactions in a 1D earth model, including non-ray theoretic effects such as diffraction and near-field effects.

REFERENCES

Balay S., K. Buschelman, V. Eijkhout, W. D. Gropp, D. Kaushik, M. G. Knepley, L. C. McInnes, B. F. Smith, and H. Zhang (2004). PETSc Users Manual, *ANL-95/11—Revision 2.1.5, Argonne National Laboratory*. http://www.mcs.anl.gov/petsc.

Chen, Y., F. Niu, R. Liu, Z. Huang, H. Tkalčić, L. Sun, and W. Chan (2010). Crustal structure beneath China from receiver function analysis, *J. Geophys. Res.* 115: B03307, doi:10.1029/2009JB006386.

Chen, P., L. Zhao, and T. H. Jordan (2007). Full-3D tomography for crustal structure in Los Angeles basin area, *Bull. Seism. Soc. Am*. 97: 1094–1120.

Chernov, L. A. (1960). Wave Propagation in a Random Medium. McGraw-Hill.

Constable, S. C., R. L. Parker, and C. G. Constable (1987). Occam's inversion: A practical algorithm for generating smooth models from electromagnetic sounding data. *Geophys.* 52: 289–300.

Dahlen, F. A. and J. Tromp (1998). Theoretical Global Seismology. Princeton, NJ: Princeton University Press.

Dalton, C. A. and G. Ekström (2006). Global models of surface wave attenuation, *J. Geophys. Res.* 111: B05317, doi:10029/2005JB003997.

Faul, U. H. and I. Jackson (2005). The seismological signature of temperature and grain size variations in the upper mantle, *Earth Planet. Sci. Lett*. 234: 119–134.

Friederich, W. (2003). The S-velocity structure of the east Asian mantle from inversion of shear and surface waveforms, *Geophys. J. Int.* 153**:** 88–102.

Gaherty, J. B., T.H. Jordan, and L .S. Gee (1996). Seismic structure of the upper mantle in a central Pacific corridor, *J. Geophys. Res.* 101: 22,291–22,309.

Gee, L. S. and T. H. Jordan (1992). Generalized seismological data functionals, *Geophys. J. Int*. 111: 363–390.

Huang, Z., W. Su, Y. Peng, Y. Zheng, and H. Li (2003). Rayleigh wave tomography of China and adjacent regions, *J. Geophys. Res.* 108: B2, 2073, doi 10.1029/2001JB001696.

Jemberíe, A. L. and B. J. Mitchell (2004). Shear-wave Q structure and its lateral variation in the crust of China and surrounding regions, *Geophys. J. Int*. 157: 363–380.

Karato, S. (1993): Importance of anelasticity in the interpretation of seismic tomography, *Geophys. Res. Lett.* 20: 1623–1626.

Katzman, R., L. Zhao, and T. H. Jordan (1998). High-resolution, two- dimensional vertical tomography of the central Pacific mantle using *ScS* reverberations and frequency-dependent travel times, *J. Geophys. Res.* 103: 17,933–17,971.

Laske, G., G. Masters, and C. Reif (2001). CRUST 2.0, A new global crustal model at 2x2 degrees, http://igppweb.ucsd.edu/~gabi/crust2.html.

Lebedev, S. and G. Nolet (2003). Upper mantle beneath southeast Asia from S velocity tomography, *J. Geophys. Res.* 108: B1, 2048, doi 10.1029/2000JB000073.

Lin, S. (2001). Comparison of digital and analog seismic recordings, *Seism. Geomagnetic Obser. Res.* 22: 57–62 (in Chinese).

Molnar, P. and P. Tapponnier (1975). Cenozoic tectionics of Asia: Effects of a continental collision. *Science* 189: 419–426.

Paige, C. C. and M. A. Saunders (1982). LSQR: Sparse linear equations and least squares problems. *ACM Trans. Math. Software* 8: 195–209.

Pei, S., J. Zhao, Y. Sun, Z. Xu, S. Wang, H. Liu, and C. A. Rowe (2007). Upper mantle seismic velocities and anisotropy in China determined through Pn and Sn tomography, *J. Geophys. Res.* 112**:** B05312, doi 10.1029/2006JB004409.

Ritzwoller, M. H., M. P. Barmin, A. Villasenor, A. L. Levshin, and E. R. Engdahl (2002). Pn and Sn tomography across Eurasia to improve regional seismic event locations, *Tectonophys.* 358: 39–55.

Sambridge, M. S. (1990). Non-linear arrival time inversion: Constraining velocity anomalies by seeking smooth models in 3-D. *Geophys. J. Int.* 102: 653–677.

Shapiro, N. M. and M. H. Ritzwoller (2002). Monte Carlo inversion for a global shear velocity model of the crust and upper mantle, *Geophys. J. Int.* 151 88–105.

Snieder, R. and A. Lomax (1996). Wavefield smoothing and the effect of rough velocity perturbations on arrival times and amplitudes. *Geophys J. Int.* 125: 796–812.

Song, Z. H., C. Q. An, G. Y. Chen, L. H. Chen, Z. Zhuang, Z. W. Fu, and J. F. Hu (1991). Study on 3-D velocity structure and anisotropy beneath the west China from the Love wave dispersion, *Acta Geophys. Sin.* 34: 694–707 (in Chinese).

Sun, Y. and M. N. Toksöz (2006). Crustal structure of China and surrounding regions from P wave traveltime tomography, *J. Geophys. Res.* 111: B03310, doi 10.1029/2005JB003962.

Sun, Y., M. N. Toksöz, S. Pei, and F. D. Morgan (2008). The layered shear-wave velocity structure of the crust and uppermost mantle in China. *Bull. Seism. Soc. Am.* 98: 746–755; DOI: 10.1785/0120050222.

Vermeesch, P. (2003). A second look at the geologic map of China: The "Sloss approach," *Int. Geol. Rev,* 45: 119–132, doi:10.2747/0020-6814.45.2.119.

Wu, F. T., A. L. Levshin, and V. M. Kozhevnikov (1997). Rayleigh wave group velocity tomography of Siberia, China and vicinity, *Pure Appl. Geophys.* 149: 447–473.

Wu, J. P., Y. H. Ming, and C. Y. Wang (2001). The S wave velocity structure beneath digital seismic stations of Yunnan province inferred from teleseismic receiver function modelling, *Chin. J. Geophys.* 44: 237–243.

Xie, J. (2006). Pn attenuation beneath Tibetan plateau, *Bull. Seismol. Soc. Am*. 97: 2040–2052; DOI: 10.1785/0120070016.

Xie, C. and A. Zhao (2003), A preliminary analysis on the waveform and magnitude from the digital and analog recordings at Huichang seismic station, *Seism. Geomagnetic Obser. Res.* 24: 39–44 (in Chinese).

Xu, G., G. Li, S. Wang, H. Chen, and H. Zhou (2000). The 3-D structure of shear waves in the crust and mantle of east continental china inverted by rayleigh wave data, *Chin. J. Geophys.* 43: 376–384.

Xu, M., L. Wang, J. Liu, K. Zhong, H. Li, D. Hu, and Z. Xu (2006). Crust and uppermost mantle structure of the Ailaoshan-Red River fault from receiver function analysis, *Sci. China Ser. D: Earth Sci.* 49: 1043.

Yin, A. and T. M. Harrison (2000). Geologic evolution of the Himalayan-Tibetan orogen, *Annu. Rev. Earth Planet. Sci*. 28: 211–280, doi:10.1146/annurev.earth.28.1.211.

Yin, A. and S. Y. Nie (1996). A Phanerozoic palinspastic reconstruction of China and its neighboring regions, in *The Tectonic Evolution of Asia*, A. Yin and T. M. Harrison, Eds. New York, NY: Cambridge University Press.

Zhao, Y., J. Jia, J. Xue, G. Liu, X. Meng, Y. Wang, and N. Song (2001). Comparison of digital and analog data from the seismic networks in Shanxi province, *Earthquake in Shanxi*, 106: 40–44 (in Chinese).

Zhao, L., T. H. Jordan, and C. H. Chapman (2000). Three-dimensional Fréchet differential kernels for seismic delay times, *Geophys. J. Int*. 141: 558–576.

Zhao, L. and T. H. Jordan (2006), Structural sensitivities of finite-frequency seismic waves: A full-wave approach. *Geophys. J. Int.* 165: 981–990.

Zou, Z. and X. Chen (2003). Mapping the crustal S-wave velocity structure by using the SV component receiver function method, *Acta Seism. Sinica* 16: 16–25.